XIV International Conference on Computational Plasticity. Fundamentals and Applications
COMPLAS XIV
E. Oñate, D.R.J. Owen, D. Peric & M. Chiumenti (Eds)

EIGENSTRAIN-BASED REDUCED ORDER HOMOGENIZATION MODELS FOR POLYCRYSTAL PLASTICITY: ADDRESSING SCALABILITY

Xiang Zhang*, **Caglar Oskay**†

*Department of Civil and Environmental Engineering
Vanderbilt University
Nashville, TN 37235
e-mail: xiang.zhang@vanderbilt.edu, web page: https://my.vanderbilt.edu/xiangzhang/

†Department of Civil and Environmental Engineering
Vanderbilt University
Nashville, TN 37235
e-mail: caglar.oskay@vanderbilt.edu, web page:https://my.vanderbilt.edu/mcml/

Key words: Sparse, Scalable, Reduced order model, Grain cluster, Multiscale model, Polycrystal plasticity

Abstract. In this manuscript, accelerated, sparse and scalable eigenstrain-based reduced order homogenization models have been developed for computationally efficient multiscale analysis of polycrystalline materials. The proposed model is based on the eigenstrain based reduced order homogenization (EHM) approach, which takes the concept of transformation field theory that pre-computes certain microscale information and considers piece-wise constant inelastic response within partitions (e.g., grains) of the microstructure for model order reduction.The acceleration is achieved by introducing sparsity into the linearized reduced order system through selectively considering the interactions between grains based on the idea of grain clustering. The proposed approach results in a hierarchy of reduced models that recovers original EHM, when full range of interactions are considered, and degrades to the Taylor model, when all grain interactions are neglected. The resulting sparse system is solved efficiently using both direct and iterative sparse solvers, both of which show significant efficiency improvements compared to the full EHM. A layer-by-layer neighbor grain clustering scheme is proposed and implemented to define ranges of grain interactions. Performance of the proposed approach is evaluated by comparison with the original full EHM and crystal plasticity finite element (CPFE) simulations.

1 INTRODUCTION

Concurrent multiscale modeling for polycrystalline materials that couples the mechanical behavior at the grain scale to structural scale poses significant challenges. First is the tremendous computational costs associated with evaluating complex polycrystalline morphologies, especially in the context of a multiscale analysis. Second is the development of constitutive models

that accurately capture the physics at the material microstructures. This manuscript addresses the former challenge.

CPFE is a powerful tool to solve various crystal plasticity problems (e.g., see Zhang and Oskay [14]). However, high computational cost of CPFE simulations on a polycrystalline representative volume element (RVE) makes its use in concurrent multiscale modeling frameworks (e.g., computational homogenization [6]) for structural scale analysis impractical. Reduced order representation of the microstructural behavior is therefore essential for structural scale analysis that takes into account the grain level behavior.

Early attempts for reduced order modeling of polycrystal plasticity are based on the iso-strain or iso-stress assumption[10, 11], which either fails compatibility or equilibrium. To overcome these drawbacks, grain-cluster [2], VPSC [5] and FFT [4] method have been developed and widely used. Eigendeformation-based reduced order homogenization (EHM) has been recently extended to polycrystal plasticity by the authors [13]. EHM is based on the transformation field theory [1] and operates in the context of computational homogenization. EHM pre-computes certain microstructure information (i.e., concentration tensors, interaction tensors) and approximates the microscale problem using a much smaller basis by prescribing spatial variation of inelastic response fields over the microstructure.

This manuscript extends the original EHM to an accelerated, sparse and scalable formulation for computationally efficient multiscale analysis of polycrystalline materials. Specifically, the grain-cluster concept is used to identify a cluster of neighboring grains for each grain, between which the interactions (i.e., short-range interactions) are considered, while interactions between grains far away from each other (i.e., long-range interactions) are neglected. Computationally, this strategy introduces sparsity into the linearized reduced order system, facilitating the use of sparse solvers. We thoroughly assessed the performance of the sparse EHM model for a range of microstructure sizes using direct and iterative sparse solvers.

2 EHM for polycrystal plasticity

EHM starts from a two-scale analysis of the governing equation, resulting in the classical form of coupled nonlinear microscale and the homogenized macroscale problem. Model order reduction is achieved by first expressing the microscale component of the displacement field in terms of "influence functions", which define its variation over the microstructure. The influence functions are numerical Green's functions computed by solving linear-elastic problems defined over the RVE prior to macroscale analysis. Next, the inelastic strain field within a microstructure are approximated by a coarse discretization. Similar to finite elements, the discretization (i.e., each coefficient) is associated with a subdomain (part) of the microstructure domain. Employing the microscale displacement discretization and the eigenstrain approximation, the reduced order microscale problem is obtained as in Box 1 (see Ref. [13] for details).

2.1 Computational Implementation Overview

The reduced order microscale system defined in Box 1 serves as the macroscale constitutive relationship and has been implemented as a User supplied MATerial (UMAT) subroutine within the finite element solver Abaqus.The constitutive equation, along with, the evolution equations for

Given: coefficient tensors $\mathbf{M}^{(\beta)}$, $\mathbf{P}^{(\alpha\beta)}$, $\mathbf{A}^{(\beta)}$, part-wise parameters $\mathbf{n}^{s(\alpha)}$, $\mathbf{m}^{s(\alpha)}$, $g_{sa}^{s(\alpha)}$, $\dot{\gamma}_0^{s(\alpha)}$, $h_0^{(\alpha)}$, $g_{s0}^{s(\alpha)}$, $\dot{\gamma}_{s0}^{(\alpha)}$, volume fraction $c^{(\beta)}$, macroscale strain $\bar{\varepsilon}_{kl}$ and its increment $\Delta\bar{\varepsilon}_{kl}$
Find: macroscale stress $\bar{\sigma}_{kl}$

• Constitutive equation:

$$M_{ijkl}^{(\beta)}\dot{\sigma}_{kl}^{(\alpha)}(\mathbf{x},t)-\sum_{\alpha=1}^{n}[P_{ijkl}^{(\alpha\beta)}-\delta^{(\alpha\beta)}I_{ijkl}]\,\dot{\mu}_{kl}^{(\alpha)}(\mathbf{x},t)=A_{ijkl}^{(\beta)}\dot{\bar{\varepsilon}}_{kl}(\mathbf{x},t)$$

$$\bar{\sigma}_{ij}=\sum_{\beta=1}^{n}c^{(\beta)}\sigma_{ij}^{(\beta)}$$

• Kinematics:

$$\dot{\mu}_{ij}^{(\alpha)}(\mathbf{x},t)=\sum_{s=1}^{N}\dot{\gamma}^{s(\alpha)}(\mathbf{x},t)\,Z_{ij}^{s(\alpha)}$$

• Flow rule:

$$\dot{\gamma}^{s(\alpha)}(\mathbf{x},t)=\dot{\gamma}_0\left(\frac{|\tau^{s(\alpha)}(\mathbf{x},t)|}{g^{s(\alpha)}(\mathbf{x},t)}\right)^{1/m}\operatorname{sgn}(\tau^{s(\alpha)}(\mathbf{x},t))$$

• Hardening rule:

$$\dot{g}^{s(\alpha)}(\mathbf{x},t)=h_0\left(\frac{g_{sa}^{s(\alpha)}-g^{s(\alpha)}(\mathbf{x},t)}{g_{sa}^{s(\alpha)}-g_0^{s(\alpha)}}\right)\sum_{s=1}^{N}|\dot{\gamma}^{s(\alpha)}(\mathbf{x},t)|$$

• Schmid's law:

$$\tau^{s(\alpha)}(\mathbf{x},t)=\boldsymbol{\sigma}^{(\alpha)}(\mathbf{x},t):\mathbf{Z}^{s(\alpha)}\quad\mathbf{Z}^{s(\alpha)}=\mathbf{n}^{s(\alpha)}\otimes\mathbf{m}^{s(\alpha)}$$

Box 1: Reduced order microscale problem.

slip and hardening constitutes a nonlinear system, evaluated using the N-R method. Evaluating the system with the part-average stresses, $\boldsymbol{\sigma}^{(\alpha)}$, as unknown, the system Jacobian is:

$$\mathbf{J}=\begin{bmatrix}
\frac{\partial\boldsymbol{\phi}^{(1)}}{\partial\boldsymbol{\sigma}^{(1)}} & \frac{\partial\boldsymbol{\phi}^{(1)}}{\partial\boldsymbol{\sigma}^{(2)}} & \cdots & \frac{\partial\boldsymbol{\phi}^{(1)}}{\partial\boldsymbol{\sigma}^{(\bar{\alpha})}} & \cdots & \frac{\partial\boldsymbol{\phi}^{(1)}}{\partial\boldsymbol{\sigma}^{(\bar{\beta})}} & \cdots & \frac{\partial\boldsymbol{\phi}^{(1)}}{\partial\boldsymbol{\sigma}^{(n)}} \\
\frac{\partial\boldsymbol{\phi}^{(2)}}{\partial\boldsymbol{\sigma}^{(1)}} & \frac{\partial\boldsymbol{\phi}^{(2)}}{\partial\boldsymbol{\sigma}^{(2)}} & \cdots & \frac{\partial\boldsymbol{\phi}^{(2)}}{\partial\boldsymbol{\sigma}^{(\bar{\alpha})}} & \cdots & \frac{\partial\boldsymbol{\phi}^{(2)}}{\partial\boldsymbol{\sigma}^{(\bar{\beta})}} & \cdots & \frac{\partial\boldsymbol{\phi}^{(2)}}{\partial\boldsymbol{\sigma}^{(n)}} \\
\vdots & \vdots & \ddots & \vdots & \ddots & \vdots & \ddots & \vdots \\
\frac{\partial\boldsymbol{\phi}^{(\bar{\alpha})}}{\partial\boldsymbol{\sigma}^{(1)}} & \frac{\partial\boldsymbol{\phi}^{(\bar{\alpha})}}{\partial\boldsymbol{\sigma}^{(2)}} & \cdots & \frac{\partial\boldsymbol{\phi}^{(\bar{\alpha})}}{\partial\boldsymbol{\sigma}^{(\bar{\alpha})}} & \cdots & \frac{\partial\boldsymbol{\phi}^{(\bar{\alpha})}}{\partial\boldsymbol{\sigma}^{(\bar{\beta})}} & \cdots & \frac{\partial\boldsymbol{\phi}^{(\bar{\alpha})}}{\partial\boldsymbol{\sigma}^{(n)}} \\
\vdots & \vdots & \ddots & \vdots & \ddots & \vdots & \ddots & \vdots \\
\frac{\partial\boldsymbol{\phi}^{(\bar{\beta})}}{\partial\boldsymbol{\sigma}^{(1)}} & \frac{\partial\boldsymbol{\phi}^{(\bar{\beta})}}{\partial\boldsymbol{\sigma}^{(2)}} & \cdots & \frac{\partial\boldsymbol{\phi}^{(\bar{\beta})}}{\partial\boldsymbol{\sigma}^{(\bar{\alpha})}} & \cdots & \frac{\partial\boldsymbol{\phi}^{(\bar{\beta})}}{\partial\boldsymbol{\sigma}^{(\bar{\beta})}} & \cdots & \frac{\partial\boldsymbol{\phi}^{(\bar{\beta})}}{\partial\boldsymbol{\sigma}^{(n)}} \\
\vdots & \vdots & \ddots & \vdots & \ddots & \vdots & \ddots & \vdots \\
\frac{\partial\boldsymbol{\phi}^{(n)}}{\partial\boldsymbol{\sigma}^{(1)}} & \frac{\partial\boldsymbol{\phi}^{(n)}}{\partial\boldsymbol{\sigma}^{(2)}} & \cdots & \frac{\partial\boldsymbol{\phi}^{(n)}}{\partial\boldsymbol{\sigma}^{(\bar{\alpha})}} & \cdots & \frac{\partial\boldsymbol{\phi}^{(n)}}{\partial\boldsymbol{\sigma}^{(\bar{\beta})}} & \cdots & \frac{\partial\boldsymbol{\phi}^{(n)}}{\partial\boldsymbol{\sigma}^{(n)}}
\end{bmatrix} \tag{1}$$

where each component is a 6×6 block expressed as:

$$\left(\frac{\partial\phi^{(\beta)}}{\partial\sigma^{(\alpha)}}\right)_{IK}=\left(\delta^{(\alpha\beta)}I_{IJ}-P_{IJ}^{(\beta\alpha)}\right)\sum_{s=1}^{N}\Omega^{s(\alpha)}Z_J^{s(\alpha)}Z_K^{s(\alpha)}+\delta^{(\alpha\beta)}\frac{M_{IK}^{(\beta)}}{\Delta t} \tag{2}$$

2.2 Analysis of EHM scalability

The efficiency of EHM compared to CPFE (i.e., ratio between simulation time of CPFE and EHM) as a function of RVE sizes is evaluated using uniaxial tension tests on a series of increasing

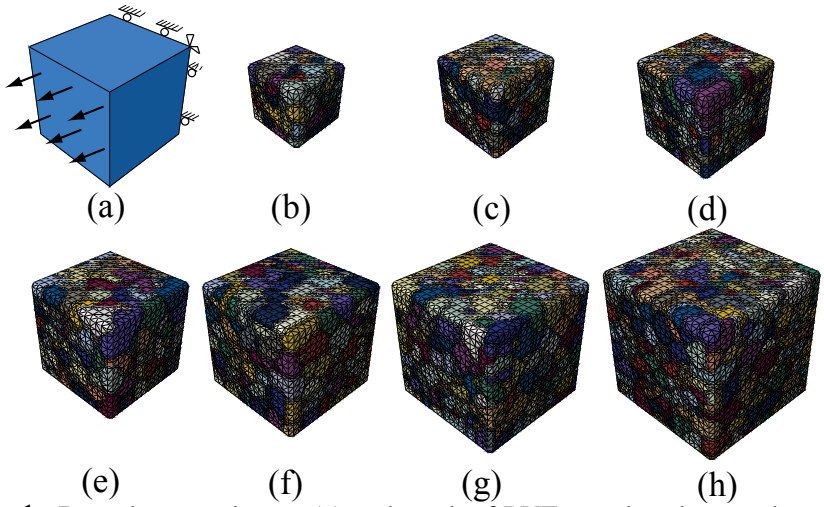

Figure 1: Boundary conditions (a) and mesh of RVEs used in the simulation with $n = 85, 154, 242, 347, 487, 629, 938$ (b-h).

Table 1: EHM efficiency compared with CPFE

n	n_{element}	n_{node}	$T_{\text{CPFE}}(s)$	$T_{\text{EHM}}(s)$	R_{DOF}	R_{Time}
85	29369	5627	2128.7	19.1	33.1	111.7
154	53149	9983	4034.0	74.85	32.4	53.9
242	84642	15583	7052.8	265.1	32.20	26.6
347	128716	23339	10371.3	662.1	33.63	15.7
487	176415	31777	13998.8	1671.5	32.63	8.4
629	238216	42651	19435.0	3434.2	33.90	5.7
938	337818	60122	29451.2	11240.6	32.05	2.6

size RVEs as shown in Fig. 1. The reduced order models consider uniform inelastic strain in each grain (i.e., n =number of grains) in the current study. The macroscale mesh consists of a single hexahedron with reduced order integration regularized by hourglass stiffness. The reference CPFE analysis is performed over the fully resolved microstructure discretized with trilinear tetrahedron elements.

The comparison between CPFE and EHM are listed in Table 1 and the efficiency of EHM compared with CPFE reduces as microstructure size increases as shown in Fig. 2. Number of grains in a RVE is often between $O(10^2)$ to $O(10^3)$ in literature. Maintaining high efficiency of EHMs with n within this range is therefore critical and motives the the current research.

The primary cause of the efficiency degradation with increasing n is the dense and unsymmetric structure of the linear system in Eq. (1), which requires $0.67(6n)^3 = 144.72n^3$ floating-point operations (FLOPs) when solved using direct solver (e.g., LAPACK LU decomposition routines). This explains the cubic increase in simulation time for the EHM as n increases.

We also investigate the effect of using iterative solver in the N-R iterations using the flexible General Minimum Residual method (FGMRES) combined with Gauss-Seidel pre-conditioning. The efficiency of EHM using FGMRES compared with CPFE is plotted in Fig. 2(b), which

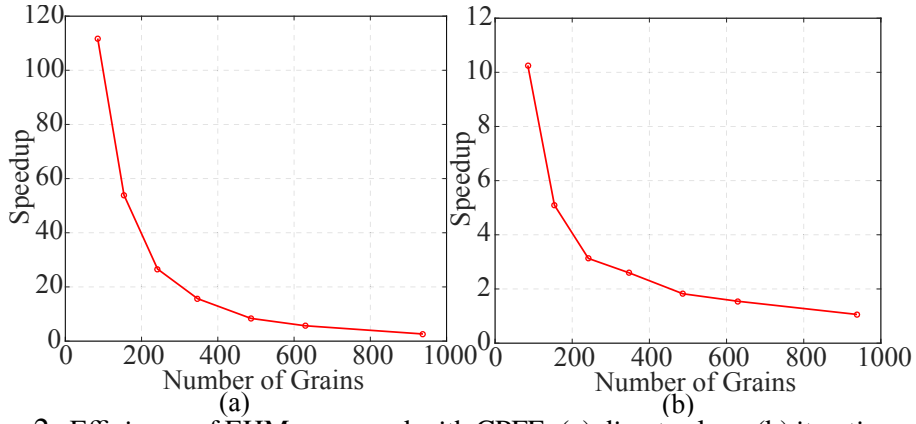

Figure 2: Efficiency of EHM compared with CPFE: (a) direct solver; (b) iterative solver.

shows lower efficiency than direct solver and similar degradation trend.

3 A sparse and scalable EHM formulation

To maintain the efficiency of EHM, one possible solution is to introduce sparsity into the linearized EHM system and decrease the FLOPs for solving the system substantially. By examing Eq. (2), one can find that, two 6×6 zero blocks will be introduced in to the Jacobian matrix (highlighted in Eq. (1)) when $\mathbf{P}^{(\bar{\alpha}\bar{\beta})} = \mathbf{P}^{(\bar{\beta}\bar{\alpha})} = \mathbf{0}$. Following this finding, a structurally symmetric sparse linear system can be obtained by setting interaction interaction tensors between a group of selected grain pairs to be zero. Zero $\mathbf{P}^{(\bar{\alpha}\bar{\beta})}$ and $\mathbf{P}^{(\bar{\beta}\bar{\alpha})}$ indicates there is no interactions between grain $\bar{\alpha}$ and $\bar{\beta}$. This section investigate the consequence of neglecting interactions between a pair of grains, $\bar{\alpha}$ and $\bar{\beta}$ and the strategy for determining a cluster of grains between which the interactions are negligible.

3.1 Coefficient tensors considering partial interactions

In the case of piecewise uniform fields, Dvorak [1] derived the following properties for the coefficient tensors:

$$\text{Kinematic consistency}: \sum_{\alpha=1}^{n} \mathbf{P}^{(\beta\alpha)} = \mathbf{I} - \mathbf{A}^{(\beta)} \tag{3}$$

$$\text{Simultaneous iso} - \text{stress/strain condition}: \sum_{\alpha=1}^{n} \mathbf{P}^{(\beta\alpha)}\mathbf{M}^{(\alpha)} = \mathbf{0} \tag{4}$$

$$\text{Elastic reciprocity}: c^{(\beta)}\mathbf{P}^{(\beta\alpha)}\mathbf{M}^{(\alpha)} = c^{(\alpha)}\mathbf{M}^{(\beta)}\mathbf{P}^{(\alpha\beta),T} \tag{5}$$

$$\text{Strain compatibility}: \sum_{\alpha=1}^{n} c^{(\alpha)}\mathbf{P}^{(\alpha\beta)} = \mathbf{0} \tag{6}$$

In addition, the concentration tensors $\mathbf{A}^{(\alpha)}$ satisfies the well-known Hill relation:

$$\sum_{\alpha=1}^{n} c^{(\alpha)}\mathbf{A}^{(\alpha)} = \mathbf{I} \tag{7}$$

In general, concentration (**A**) and interaction tensors (**P**) are computed from the elastic Green's function through linear elastic analysis on the microstructure domain. Our goal here is to derive a new set of coefficient tensors from the original ones when interaction between a chose pair of grains are neglected that enforce Eqs. (3)-(7) as much as possible. By applying this formulation on a group of selected grains, one can obtain a sparse EHM model.

While enforcing Eqs. (3)- (7) simultaneously is not successful to the best knowledge of the authors, we now introduce two models that will either enforce the kinematic consistency or simultaneous iso-stress/strain condition, namely kinematically (ϵ-EHM) and simultaneous iso-stress/strain constrained sparse EHM (σ-EHM), respectively. For both models, the compliance tensors remain unchanged. The new coefficient tensors for ϵ-EHM are:

$$\mathbf{P}'^{(\alpha\beta)} = \begin{cases} \mathbf{0} & \{\alpha,\beta\} = \{\bar{\alpha},\bar{\beta}\} \\ \mathbf{P}^{(\bar{\alpha}\bar{\alpha})} + \frac{c^{(\bar{\beta})}}{c^{(\bar{\alpha})}}\mathbf{P}^{(\bar{\beta}\bar{\alpha})} & \{\alpha,\beta\} = \{\bar{\alpha},\bar{\alpha}\} \\ \mathbf{P}^{(\bar{\beta}\bar{\beta})} + \frac{c^{(\bar{\alpha})}}{c^{(\bar{\beta})}}\mathbf{P}^{(\bar{\alpha}\bar{\beta})} & \{\alpha,\beta\} = \{\bar{\beta},\bar{\beta}\} \\ \mathbf{P}^{(\alpha\beta)} & \text{otherwise} \end{cases} \tag{8}$$

$$\mathbf{A}'^{(\alpha)} = \begin{cases} \mathbf{A}^{(\alpha)} & \alpha \notin \{\bar{\alpha},\bar{\beta}\} \\ \mathbf{A}^{(\bar{\alpha})} + \mathbf{P}^{(\bar{\alpha}\bar{\beta})} - \frac{c^{(\bar{\beta})}}{c^{(\bar{\alpha})}}\mathbf{P}^{(\bar{\beta}\bar{\alpha})} & \alpha = \bar{\alpha} \\ \mathbf{A}^{(\bar{\beta})} + \mathbf{P}^{(\bar{\beta}\bar{\alpha})} - \frac{c^{(\bar{\alpha})}}{c^{(\bar{\beta})}}\mathbf{P}^{(\bar{\alpha}\bar{\beta})} & \alpha = \bar{\beta} \end{cases} \tag{9}$$

while the coefficient tensors for σ-EHM are:

$$\mathbf{P}'^{(\alpha\underline{\beta})} \begin{cases} \mathbf{0} & \{\alpha,\beta\} = \{\bar{\alpha},\bar{\beta}\} \\ \mathbf{P}^{(\bar{\alpha}\bar{\alpha})} + \frac{c^{(\bar{\beta})}}{c^{(\bar{\alpha})}}\mathbf{M}^{(\bar{\alpha})}\mathbf{P}^{(\bar{\beta}\bar{\alpha}),T}\mathbf{M}^{(\bar{\alpha}),-1} & \{\alpha,\beta\} = \{\bar{\alpha},\bar{\alpha}\} \\ \mathbf{P}^{(\bar{\beta}\bar{\beta})} + \frac{c^{(\bar{\alpha})}}{c^{(\bar{\beta})}}\mathbf{M}^{(\bar{\beta})}\mathbf{P}^{(\bar{\alpha}\bar{\beta}),T}\mathbf{M}^{(\bar{\beta}),-1} & \{\alpha,\beta\} = \{\bar{\beta},\bar{\beta}\} \\ \mathbf{P}^{(\alpha\beta)} & \text{otherwise} \end{cases} \tag{10}$$

$$\mathbf{A}'^{(\underline{\alpha})} \begin{cases} \mathbf{A}^{(\alpha)} & \alpha \notin \{\bar{\alpha},\bar{\beta}\} \\ \mathbf{A}^{(\bar{\alpha})} + \mathbf{P}^{(\bar{\alpha}\bar{\beta})} - \frac{c^{(\bar{\beta})}}{c^{(\bar{\alpha})}}\mathbf{M}^{(\bar{\alpha})}\mathbf{P}^{(\bar{\beta}\bar{\alpha})}\mathbf{M}^{(\bar{\alpha}),-1} & \alpha = \bar{\alpha} \\ \mathbf{A}^{(\bar{\beta})} + \mathbf{P}^{(\bar{\beta}\bar{\alpha})} - \frac{c^{(\bar{\alpha})}}{c^{(\bar{\beta})}}\mathbf{M}^{(\bar{\beta})}\mathbf{P}^{(\bar{\alpha}\bar{\beta})}\mathbf{M}^{(\bar{\beta}),-1} & \alpha = \bar{\beta} \end{cases} \tag{11}$$

Remark. *ϵ-EHM can be deemed as a model between Taylor model and full EHM. It can be shown, when all transmitted interactions are neglected ($\mathbf{P}^{(\alpha,\beta)} = \mathbf{0}$, $\alpha \neq \beta$), the self-induced interaction tensors become zero and concentration tensors will become identity tensor, leading to a diagonal system in Eq.* (2) *and recovers the classical Taylor model.*

3.2 A consistent grain clustering scheme

In the current study, we employe a nearest neighbor based algorithm to consistently eliminate weak interactions between grains that are far from each other. Let $\Theta_1^{(\alpha)}$ denote the domain of all grains in the immediate neighborhood of the grain, α, with domain, $\Theta^{(\alpha)}$. The immediate neighborhood of $\Theta_1^{(\alpha)}$ is denoted as $\Theta_2^{(\alpha)}$ and constitutes the secondary influence zone of grain

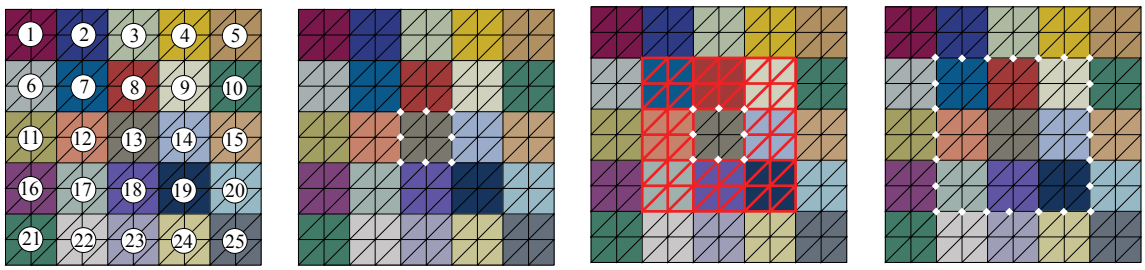

Figure 3: Schematic demonstration of the clustering scheme.

α. Following the same argument for higher order influence zones, n_c-layer grain cluster for grain α is defined as:

$$\Omega_{n_c}^{(\alpha)} = \Theta^{(\alpha)} \bigcup_{i=1}^{n_c} \Theta_i^{(\alpha)} \tag{12}$$

The algorithm for constructing the grain clusters is schematically illustrated in Fig. 3. The index of each grain is illustrated in Fig. 3(a). For each grain within the microstructure, the boundary nodes are identified (Fig. 3(b)). An element connectivity based search is conducted to identify all grains that contain at least one of the boundary nodes to build $\Theta_1^{(\alpha)}$ (Fig. 3(c)). To build the second layer of neighbors, $\Theta_2^{(\alpha)}$, the above process is repeated by replacing $\Theta^{(\alpha)}$ with $\Theta_1^{(\alpha)}$ (Fig. 3(d)).

4 Computational implementation

The nonlinear numerical procedures for the sparse EHM models are similar to the full EHM (detailed in Ref. [13]). The characteristics of the linearized equations of the sparse EHM system is exploited to efficiently evaluate the reduced order models. In particular, we leverage the structural symmetry (Fig. 4(a)-(b)), sparsity, compressed storage and reordering (Fig. 4(c)-(d)) of the equation system for computational efficiency.

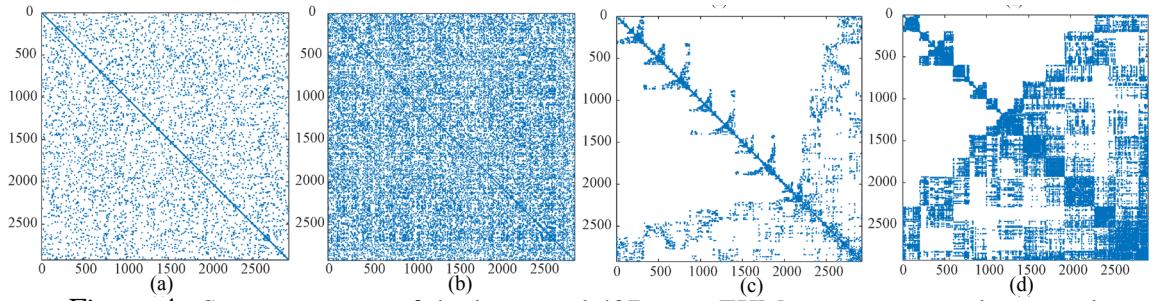

Figure 4: Sparsity pattern of the linearized 487-grain EHM system: original one- and two-layer sparse EHM and their reordered versions (c)-(d).

The implementation is performed in two stages: (1) preprocessing; and (2) multiscale analysis. Particular attention is paid on obtaining as much information as possible in the preprocessing stage (e.g., CRS format and reordering as well as analysis and symbolic factorization in the case

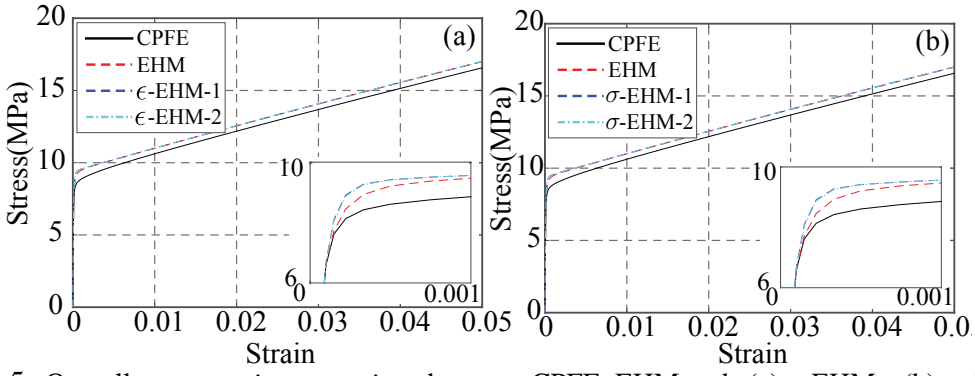

Figure 5: Overall stress-strain comparison between CPFE, EHM and: (a) ϵ-EHMs; (b) σ-EHMs.

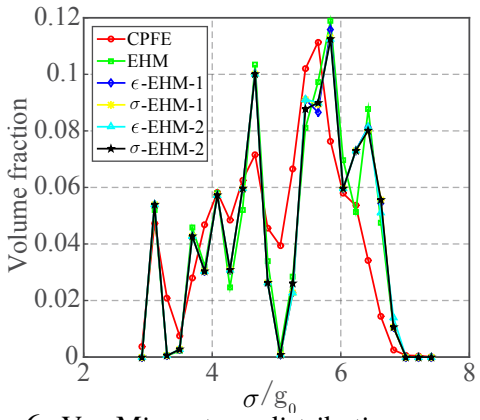

Figure 6: Von Mises stress distribution comparison.

of direct solver) and directly use them in the later on N-R process since the sparsity pattern of the system remain unchanged. Both direct (PARDISO) and iterative solver (FGMRES) are implemented for maximum efficiency (parallel disabled) in the multiscale analysis stage and the details are skipped here for simplicity.

5 Numerical verification

5.1 Accuracy and efficiency evaluation

The material considered is pure aluminum with material parameters from Ref. [13]. The RVE is taken to consist of 487 grains and the microstructure is shown in Fig. 1(f) under uniaxial tension. The overall stress-strain response obtained by the CPFE, full EHM, ϵ-EHM and σ-EHM models are compared in Fig. 6. Both ϵ-EHM and σ-EHM models provide almost identical results as the full EHM model. The local von Mises stress distribution (i.e., stress distribution of all the grains within the RVE, normalized by g_0) computed with the CPFE and the proposed models within the RVE is plotted in Fig. 6. The discrepancies between the stress distribution for different EHMs are negligible, and the distribution match the results from the reference CPFE simulation with reasonable accuracy.

The efficiency characteristics of the EHM models are assessed by performing simulations with microstructures shown in Fig. 1. The speedup of different EHM models compared with

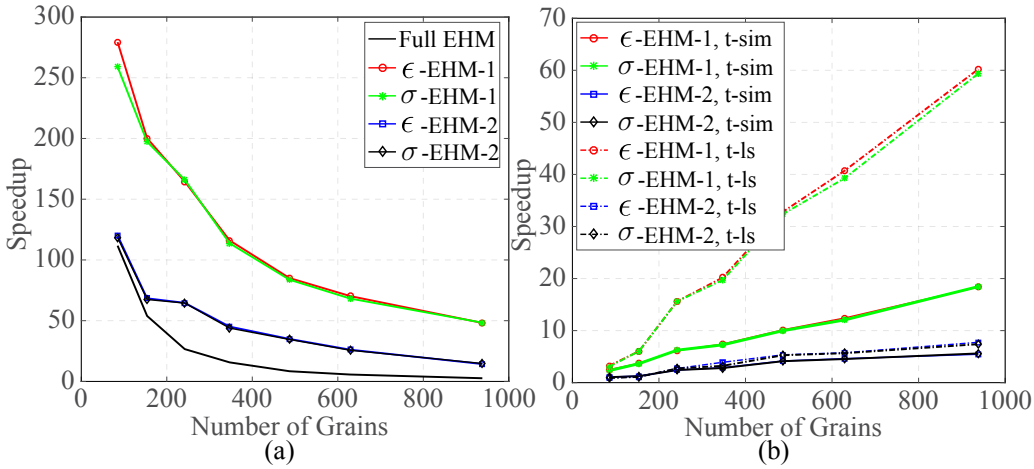

Figure 7: Efficiency comparison: (a) full and sparse EHMs compared with CPFE; (b) sparse EHM compared with full EHM.

CPFE are listed in Table 1 and plotted in Fig. 7. One-layer sparser EHMs (ϵ-EHM-1 and σ-EHM-1) provide significant speedup compared with full EHM and a much slower efficiency degradation as the microstructure size increases.

The speedup of sparse EHMs compared with the full EHM are plotted in Fig. 7(b), together with the the speedup of linear solver portion (accumulated CPU time spent for linear solver only). It is observed that the speedup of one-layer sparse EHM compared with full EHM increases linearly as n increases. The speedup of the two-layer sparse EHM compared with EHM, shows a sub-linear relationship with n. This is because sparsity decreases fast from the one-layer sparse EHM to the two-layer sparse EHM and the FLOPs of solving a sparse linear system increase fast as the decrease of the sparsity. The behavior of speedup for the linear solver portion is generally similar to the total simulation times, but the curves show much higher slopes. This is because the other procedures (i.e., computation of slip resistance evolution, matrix constructions etc.) are of similar order for all models, including the full EHM and sparse EHM.

Figure 8 shows the efficiency of ϵ-EHM-1 using the iterative solver as a function of n. It clearly shows that sparsity also significantly increase the efficiency of EHM when using iterative solver, while the speedup is less than the case of direct solver in the cases we studied.

5.2 A structural example: plate with hole under bolt load

To demonstrate the capability of sparse EHM in solving structural scale problems, we investigated the response of a plate subjected to bolt pressure as shown in Fig. 9(a). Half of the plate is discretized due to symmetry with 27,680 tri-linear eight-noded hexahedron elements (Fig. 9(b)). The microstructure is the 938-grain RVE as shown in Fig. 1 (h). The simulation therefore tracks 25,963,840 grains throughout the domain of the plate and the one-layer ϵ-EHM is used in this study.

The stress-contour of the plate at the end of loading is shown in Fig. 9(c). The reaction force versus the displacement at the far end (i.e., $\theta = 0^o$) of the hole is shown in Fig. 10(a). 12 elements at each position as shown in Fig. 9(a) are selected (probing 11,256 grains at each

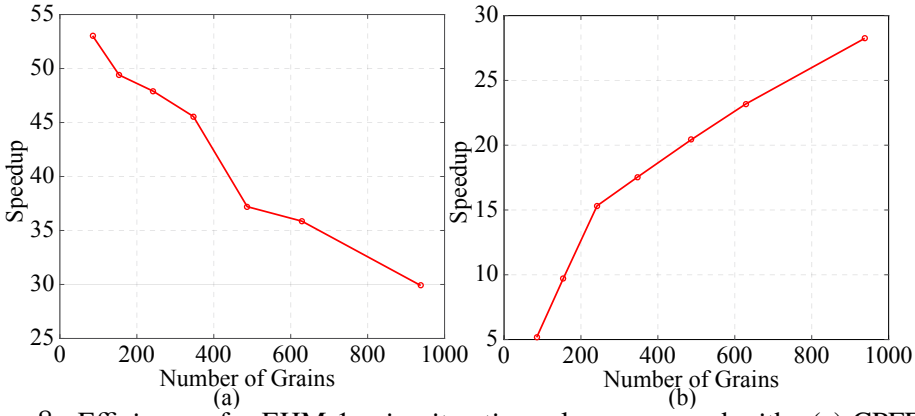

Figure 8: Efficiency of ϵ-EHM-1 using iterative solver compared with: (a) CPFE and (b) full EHM using iterative solver.

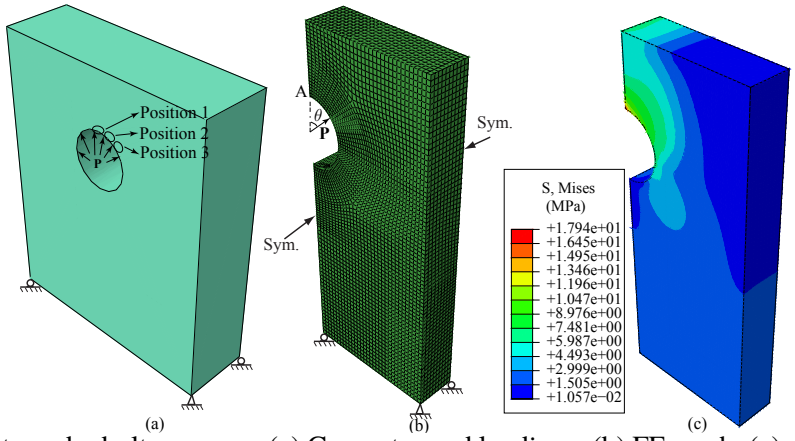

Figure 9: Plate under bolt pressure: (a) Geometry and loadings; (b) FE mesh; (c) stress contour.

position), and the von Mises stress (normalized by initial slip resistance, g_0) histograms of the microscale grains at each position are plotted in Fig. 10(b). Microscale stress histograms show a decreasing grain level von Mises stress from position 1, 2 to 3, consistent with the macroscale stress at position 1, 2 and 3 as shown in Fig. 9(c).

6 Conclusions and future research interests

We presented a grain-cluster accelerated eigenstrain-based reduced-order homogenization model for computationally efficient modeling of complex polycrystal microstructures through selectively considering grain-to-grain interactions. It is found that the proposed sparse EHM can maintain the high efficiency better as the RVE size increases and with negligible differences compared with full EHM for both overall stress-strain response and local response. The concept of the sparse EHM is also beneficial for other reduced models (e.g., [9, 7, 8, 3, 12]) when higher resolution (i.e., number of parts is relative large) is required. Future work will consider incorporating of the sparse EHM concept into these models for efficiency improvement.

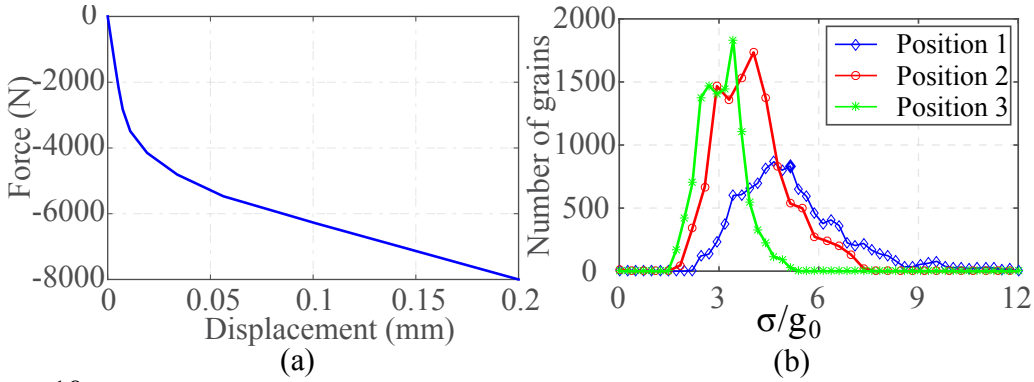

Figure 10: Response of the plate: (a) force-displacement; (b) local von Mises stress histogram.

References

[1] G. J. Dvorak. Transformation field analysis of inelastic composite materials. *Proc. Math. Phys. Eng. Sci.*, 437:311–327, 1992.

[2] P. V. Houtte. On the equivalence of the relaxed taylor theory and the bishop-hill theory for partially constrained plastic deformation of crystals. *Mater. Sci. Eng*, 55:69–77, 1982.

[3] T. Hui and C. Oskay. A high order homogenization model for transient dynamics of heterogeneous media including micro-inertia effects. *Comput. Methods Appl. Mech. Engrg.*, 273:181–203, 2014.

[4] R. A. Lebensohn. N-site modeling of a 3d viscoplastic polycrystal using fast fourier transform. *Acta Mater.*, 49:2723–2737, 2001.

[5] R.A. Lebensohn and C.N. Tome. A self-consistent anisotropic approach for the simulation of plastic deformation and texture development of polycrystals: Application to zirconium alloys. *Acta Meta. Mater.*, 41:2611–2624, 1993.

[6] C. Miehe, J. Schroder, and J. Schotte. Computational homogenization analysis in finite plasticity simulation of texture development in polycrystalline materials. *Comput. Methods Appl. Mech. Engrg.*, 171:387–418, 1999.

[7] C. Oskay. Variational multiscale enrichment for modeling coupled mechano-diffusion problems. *Int. J. Numer. Meth. Engng*, 89:686–705, 2012.

[8] C. Oskay. Variational multiscale enrichment method with mixed boundary conditions for modeling diffusion and deformation problems. *Comput. Methods Appl. Mech. Engg.*, 264: 178–190, 2013.

[9] C. Oskay and M. Haney. Computational modeling of titanium structures subjected to thermo-chemo-mechanical environment. *Int. J. Solids Struct.*, 47(24):3341–3351, 2010.

[10] G. Sachs. Zur ableitung einer fliessbedingung. *Ver. Dtsch. Ing.*, 72:734–736, 1928.

[11] G.I. Taylor. Plastic Strain in Metals. *J. Inst. Met.*, 62:307–324, 1938.

[12] S. Zhang and C. Oskay. Reduced order variational multiscale enrichment method for elasto-viscoplastic problems. *Comput. Methods Appl. Mech. Engg.*, 300:199–224, 2016.

[13] X. Zhang and C. Oskay. Eigenstrain based reduced order homogenization for polycrystalline materials. *Comput. Methods Appl. Mech. Engrg.*, 297:408–436, 2015.

[14] X. Zhang and C. Oskay. Polycrystal plasticity modeling of nickel-based superalloy in 617 subjected to cyclic loading at high temperature. *Modelling Simul. Mater. Sci. Eng.*, 24: 055009, 2016.